One-step synthesis of nanocarbon-decorated MnO$_2$ with superior activity for indoor formaldehyde removal at room temperature

Fang Liu[a], Shaopeng Rong[a,b], Pengyi Zhang[a,b,c,*], Lele Gao[a,c]

[a] *State Key Joint Laboratory of Environment Simulation and Pollution Control, School of Environment, Tsinghua University, Beijing 100084, China*
[b] *Laboratory of Solid Waste Management and Environment Safety (Tsinghua University), Ministry of Education, Tsinghua University, Beijing 100084, China*
[c] *Beijing Key Laboratory for Indoor Air Quality Evaluation and Control, Beijing 100084, China*

ARTICLE INFO

ABSTRACT

Indoor formaldehyde (HCHO) pollution receives wide concerns, it is still a challenge to remove low-level HCHO at high gas-hourly space velocity (GHSV) at room temperature required in the indoor environment. Thus, a graphite-like nanocarbon decorated MnO$_2$ (GLC-MnO$_2$) was synthesized with a rapid one-step procedure, i.e., a redox reaction between potassium manganese and glucose at 80 °C for 15 min. The as-synthesized GLC-MnO$_2$ hybrid showed excellent activity for HCHO removal and its mineralization to CO$_2$ at room temperature. Under the GHSV of 600 L/g$_{cat}$ h, the single-pass removal efficiency was as high as ~92% for 0.5 mg/m^3 HCHO and ~89% for 1.0 mg/m^3 HCHO, which is much higher than those previously achieved by MnO$_2$-based catalysts. Furthermore, its room-temperature activity was little influenced by the relative humidity in the wide range of 4%–80%. The significantly enhanced catalytic performance of GLC-MnO$_2$ could be attributed to abundant Mn vacancies and surface adsorbed active oxygen resulted from the coexisted nanocarbon which in-situ formed during preparation of GLC-MnO$_2$. The presence of nanocarbon may also facilitate electron transfer to form reactive oxidation species for HCHO oxidation. The present study provides a new route to develop efficient catalyst for indoor air pollutants removal.

1. Introduction

Building related illness (BRI) is a widely concerned problem, which is partly caused by the exposure to airborne contaminants such as benzene, toluene and formaldehyde (HCHO) [1–3]. Occupants may suffer from a series of symptoms of diagnosable, including nausea; irritation of eyes, nose and throat; headaches, mental fatigue and even cancer. HCHO is one of the most representative and ubiquitous indoor air pollutants. The International Agency for Research on Cancer (IARC) classified HCHO as carcinogenic to humans (Group 1) based on sufficient evidence in humans and in experimental animals [2,4]. HCHO is an important chemical feedstock. Due to its economic importance and widespread use, many people are exposed to HCHO environmentally and/or occupationally [2].

Hence, in recent years many researchers have tried to develop efficient methods for HCHO removal [5–7]. Among them, catalytic oxidation is considered as the most promising technology without secondary pollution. Supported noble metals (e.g., Pt, Pd, Au and Ag) materials have been widely investigated and showed capability to completely decompose HCHO into CO$_2$ at room temperature [8–11].

Recently, He's group further increased the activity of supported noble metal (Pt or Pd) with assistance of alkaline metals to improve the dispersion of noble metal on the supporting material [12,13]. However, noble metal catalysts are limited by their high cost and scarcity in the practical application. Alternatively, manganese oxides and other transitional metal oxides have been proven to efficiently decompose HCHO at low temperatures [14,15]. Zhang et al. [16] found that δ-MnO$_2$ showed the best catalytic activity, achieving almost 100% conversion of 170 ppm HCHO at 80 °C and 35% conversion at 50 °C under the gas hourly space velocity (GHSV) of 100 L/g$_{cat}$ h. Tian et al. [17] synthesized two porous MnO$_2$ nanomaterials and found the K-OMS-2 nanoparticles could oxidize more than 64% HCHO (460 ppm) into CO$_2$ at 100 °C and only 10% HCHO converted to CO$_2$ in the range of 20–40 °C. The poor activity at room temperature hinder the practical application in indoor environment.

Researchers have taken some strategies to promote the catalytic activity of MnO$_2$, such as doping with transition metals and hybrid carbon. Tang et al. [18] prepared MnO$_x$-CeO$_2$ mixed oxide catalyst by several methods and found the MnO$_x$-CeO$_2$ obtained by modified co-precipitation method showed ~27% HCHO conversion (HCHO:

580 ppm) at 60 °C under the GHSV of 21 L/g$_{cat}$ h. Our group [19] synthesized Ce-MnO$_2$ catalyst with lower Ce/Mn ratio of 1:10, which exhibited the HCHO conversion of ~23% (HCHO: 190 ppm) at 50 °C under the GHSV of 90 L/g$_{cat}$ h. The above transition metal doped MnO$_2$ achieved complete oxidation of hundreds of ppm HCHO at high temperature (i.e., 100 °C) and low GHSV. Lu et al. [20] assembled the MnO$_2$ onto the graphene nanosheets forming graphene-MnO$_2$ hybrid nanostructure, which achieved complete oxidation of HCHO (100 ppm) at 65 °C and 20% at 30 °C under the GHSV of 30 L/g$_{cat}$ h. As a matter of fact, the high concentration HCHO test is far from the real indoor environment, where the HCHO concentration is at low level (e.g., 0.01–1 mg/m^3). Thus, it is more meaningful to evaluate the performance of transition metal oxides such as MnO$_2$ to remove low-level HCHO at room temperature.

There are few literatures to report the room-temperature degradation of low-concentration HCHO, which is normally encountered in the indoor environment. Shi's group [21] reported that MnO$_x$ coated on honeycomb ceramics exhibited 30% conversion of 1 ppm HCHO under the space velocity of ~48,000 h^{-1} with the total HCHO removal amount of 11.87 mg/g$_{cat}$. Our group [22] developed the composite MnO$_x$/granular activated carbon, which achieved 75% conversion of 0.5 mg/m^3 HCHO under the GHSV of 120 L/g$_{cat}$ h during 30 h period. Zhu et al. [19] reported that the Ce-MnO$_2$ catalyst exhibited the ~53% removal ratio for 0.5 mg/m^3 HCHO under the GHSV of 600 L/g$_{cat}$ h. Wang et al. [23] prepared MnO$_x$/PET by one-step method, which achieved over 94% conversion of ~0.6 mg/m^3 HCHO within 10 h under the space velocity ~17,000 h^{-1} and relative humidity (RH) ~50%.

To meet the increasing demand on indoor HCHO removal and to improve the activity of catalysts at room temperature and high GHSV condition required by the indoor air cleaning, in the present work, we developed a novel strategy to synthesize a graphite-like nanocarbon decorated-MnO$_2$ (GLC-MnO$_2$) hybrid material. The nanocarbon and MnO$_2$ were simultaneously formed and intermixed by a facile one-step synthesis procedure, i.e., in which potassium permanganate reacted with glucose at 80 °C for 15 min. The GLC-MnO$_2$ composite material exhibited superior activity at room temperature for low-level (close to real level in indoor environment) HCHO under the high space velocity, reaching ~90% conversion of 0.3–1.0 mg/m^3 HCHO under the GSHV of 600 L/g$_{cat}$ h in a wide range of RH (4–80%).

2. Experimental section

2.1. Synthesis of carbon decorated MnO$_2$

The carbon decorated-MnO$_2$ composite was synthesize with a facile reaction between potassium permanganate (KMnO$_4$) with glucose or sucrose. Typically, 1.2 g KMnO$_4$ was first dissolved in 100 mL deionized water in a conical flask to get a purple solution. Then, 0.18 g glucose or 0.34 g sucrose was added into the above purple solution. The conical flask was kept in a water bath at 80 °C for 15 min. Owing to the strong oxidizing property of KMnO$_4$, the glucose or sucrose was oxidized into carbon species, and brown MnO$_2$ simultaneously formed. The brown precipitate was centrifuged and washed three times with deionized water and then dried in an oven at 105 °C for 12 h. The final products synthesized with glucose and sucrose were referred to as GLC-MnO$_2$ and AC-MnO$_2$, respectively.

2.2. Characterization

X-ray diffraction (XRD) analyses were performed on a Rigaku D/max-2500/PC diffractometer (Japan) using Cu Kα radiation by step scanning with a scan rate of 0.2°/s. A field-emission scanning electron microscope (SEM) instrument (S-5500, HITACHI, Japan) was applied to observe the morphology of catalysts. Transmission electron microscopy (TEM) observation was conducted on a JEM-2010F JEOL (Japan)

operated at 200 kV. Energy dispersive X-ray spectroscopy (EDX) measurements were performed on a Philips EDAX instrument.

Fourier transform infrared spectroscopy (FTIR) was recorded on a Thermo Nicolet NEXUS-870 spectrophotometer in the wavenumber ranging from 4000–400 cm^{-1}. Raman measurements were carried out with a 532 nm laser and a power of 0.1 mW on a Renishaw Raman spectrophotometer with an inVia reflex optical microscope (Britain). The Brunauer–Emmett–Teller (BET) specific surface area was measured by nitrogen physisorption at liquid nitrogen temperature (77 K) on a Micromeriticis ASAP 2020 analyzer (USA). All the samples were degassed at 250 °C for 4 h before testing. The total specific surface area was determined by a multipoint BET method, and the pore size distributions were calculated using the adsorption branches of N$_2$ adsorption-desorption isotherms by BJH method. The electron spin resonance (ESR) signals of radicals were examined on a JES-FA200 ESR spectrometer by using 5,5-dimethyl-l-pyrroline N-oxide (DMPO) as a spin-trap reagent for radical measurements. 50 mM DMPO was used to trap the hydroxyl radicals (·OH) and superoxide anion radicals (·O$_2$$^-$) of the samples (0.12 g/mL), producing the adducts of DMPO-·OH in aqueous suspension and DMPO-O$_2$$^-$ in methanol suspension, respectively. Electrochemical measurements were carried out with an electrochemistry workstation (PARSTAT2273) in a conventional three-electrode system. A platinum wire was used as a counter electrode; a saturated calomel electrode was used as a reference electrode; and a catalyst modified glassy carbon electrode was used as a working electrode. Before modification, each glassy carbon electrode was sequentially polished with 0.3 and 0.05 µm Al$_2$O$_3$ powder, rinsed with water and dried in air. Then 5 mg catalyst powder was mixed with 0.5 wt% Nafion/isopropanol solution. 10 µL of the ink suspension solution was deposited onto the surface of the grassy carbon electrode, and then dried at room temperature. Finally, three electrodes were immersed in 1 M Na$_2$SO$_4$ electrolyte for testing. Charge-discharge measurements were performed at a constant current density of 2 mA/cm^2 over the same operating potential range.

X-ray photoelectron spectroscopy (XPS) analyses were performed on a Thermo Scientific ESCALAB 250Xi. The energy positions of the peaks were calibrated by fixing the position of C 1s peak at 284.6 eV. H$_2$ temperature programmed reduction (H$_2$-TPR) and O$_2$ temperature programmed desorption (O$_2$-TPD) were performed in an AutoChem 2920 instrument (Micromeritics, USA), equipped with a TCD detector. In a typical experiment, ~50 mg sample (40–60 meshes) was placed in a U-type quartz tube. First, the sample was pretreated by helium gas (50 mL/min) for 30 min at 105 °C, then it was cooled down to 40 °C in the helium gas. For H$_2$-TPR experiment, the sample was reduced by the 5% H$_2$/Ar (50 mL/min) from 40 to 500 °C with a heating rate of 5 °C/min. The H$_2$ consumption was detected by the TCD detector. For O$_2$-TPD experiment, the sample was treated by 5% O$_2$/Ar (50 mL/min) for 30 min after pretreatment. Then, the sample was purged with helium flow for 30 min to remove the physiosorbed O$_2$ and stabilize the baseline. Subsequently, the sample was heated from 40 to 800 °C with a heating rate of 5 °C/min in the helium stream (50 mL/min). The O$_2$ desorption was detected by the TCD detector.

In-situ diffuse reflectance infrared fourier transform spectrometry (DRIFTS) was recorded on a Nicolet 6700 FTIR spectrometer (USA) equipped with a MCT detector and a high temperature reaction chamber with ZeSe windows. The reaction chamber provides all necessary gas in- and outlets and allows for the temperature measurement and control. Catalyst samples were placed in the reaction chamber and the temperatue was controlled at 25 °C. The 30 mL/min of HCHO (~80 ppm) was injected into the chamber with the synthetic air (79% N$_2$/21% O$_2$) as the balance gas. The spectra were obtained with a resolution of 4 cm^{-1} and an accumulation of 64 scans, with spectra recorded at time interval of 5 min.

2.3. Evaluation of activity for HCHO removal

The activity for HCHO removal was evaluated with both staic and dynamic test modes at 25 °C. The static test was used to evaluate the activity of as-synthesizd samples for high HCHO removal and simultaneous conversion to CO_2 according to the literature [24]. Briefly, 100 mg of sample was put in a 3.5 L organic glass reactor. The reactor was flushed with CO_2-free synthetic air for 15 min to eliminate the interference of atmospheric CO_2 on the measurement of CO_2 formation, and the initial concentration of HCHO was adjusted to ~200 ppm. The change of HCHO concentration was monitored with PN-2000 HCHO online detector (PNLE, Shenzhen), and the CO_2 was determined on-line by a gas chromatograph (GC-2014, Shimadzu) equipped with a methanizer and an FID detector.

The dynamic test was used to evaluate the activity for low-concentration HCHO close to the real pollution level accounted in the indoor environment. 100 mg sample with the size of 40–60 meshes was placed in a quartz tube with the inner diameter of 6 mm. The inlet HCHO concentration was set at $0.5 \, mg/m^3$ or $1.0 \, mg/m^3$. The total flow rate was 1 L/min, with the corresponding GHSV of $600 \, L/g_{cat} \, h$. HCHO was generated by flowing compressed air over formaldehyde solution kept in a thermostated water bath. The relative humidity was adjusted by passing compressed air through a bubbler kept in a water bath at room temperature. The relative humidity was measured by using humidity equipment (TES 1360A humidity temperature meter). Both the inlet and outlet concentration of HCHO was determined by MBTH method [19]. The HCHO removal efficiency was calculated as follow:

$$\text{Removal efficiency (\%)} = \frac{[HCHO]_{in} - [HCHO]_{out}}{[HCHO]_{in}} \times 100\%$$

where $[HCHO]_{in}$ and $[HCHO]_{out}$ are the inlet and outlet HCHO concentration, respectively.

3. Results and discussion

3.1. Crystal structure and morphology

Fig. 1 shows the powder XRD patterns of as-prepared carbon modified MnO_2. Both samples presented the diffraction peaks centering at around 12.3°, 24.6°, 36.5° and 65.5°, which can be assigned to the (001), (002), (100) and (110) planes of the birnessite-type MnO_2 (JCPDS No. 80-1098) [25]. The peaks of both samples were broad and weak, implying their poor crystallinity. Besides, the GLC-MnO_2 had the weaker intensity than AC-MnO_2, which means GLC-MnO_2 owned even poorer crystallinity and more defects.

The morphology and structure of two samples were observed by SEM. As shown in Fig. 2a and e, both catalysts seemed like hierarchical
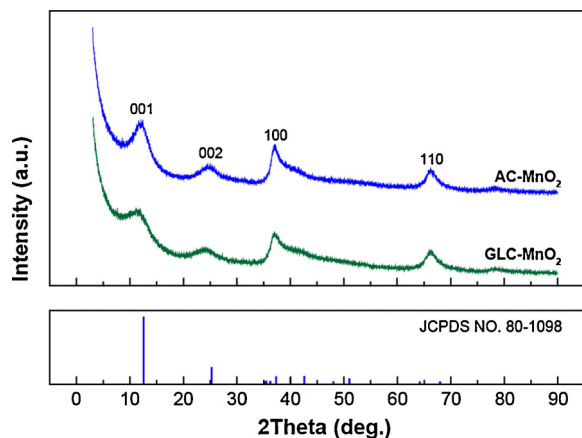

Fig. 1. Powder XRD patterns of the GLC-MnO_2 and AC-MnO_2.

nanospheres assembled with irregular MnO_2 nanosheets. The size of GLC-MnO_2 nanoflowers was ~30–80 nm (Fig. 2a), while AC-MnO_2 showed a tight packed agglomeration with much larger size of ~150–200 nm (Fig. 2e). The GLC-MnO_2 were disordered porous superstructures with highly rough outer surface, the smaller particles could expose more active sites for catalytic reaction. The BET surface area of GLC-MnO_2 was $216.0 \, m^2/g$, which was much larger than that of AC-MnO_2 ($70.3 \, m^2/g$), as shown in Table 1.

TEM observation further revealed the microstructure of the hybrid materials. As shown in Fig. 2b, GLC-MnO_2 owned loose and porous structure, while AC-MnO_2 seemed much compact (Fig. 2f). From HR-TEM image of GLC-MnO_2 (Fig. 2c), it can be clearly seen that uniform spherical nanoparticles intermixed and decorated with the amorphous components. The corresponding lattice space of 0.21 nm could be identified, which could be assigned to the (100) diffraction facet of graphene [26,27]. In addition to a part of amorphous and blur area observed in Fig. 2c, the other lattice space of 0.24 nm could be identified on the larger grains, which is consistent with the lattice spacing of (110) planes of δ-MnO_2 [28,29]. The elemental mappings were conducted to learn the distribution of Mn, O, K and C. It can be seen from Fig. 2d that carbon element was in a pretty high dispersion degree as well as Mn, O and K. The above results reveal that during synthetic reaction of permanganate with glucose, potassium permanganate was reduced into weakly-crystalized δ-MnO_2, simultaneously glucose partly transformed into graphite-like nanocarbon particles, which intermixed with δ-MnO_2 to form irregular nanosheets of GLC-MnO_2 composites. If sucrose was used as reductant precursor, as shown in Fig. 2g, only the lattice spacing of 0.24 nm ascribed to δ-MnO_2 could be observed on AC-MnO_2, and no lattice fringe ascribed to the graphite-carbon could be found. However, as shown in Fig. 2h, the carbon element also homogeneously distributed in the AC-MnO_2 sample, which implied amorphous carbon intermixed with δ-MnO_2 particles in the AC-MnO_2 sample.

As we reported previously [19], the doping of cerium inhibited the growth of MnO_2 crystal and resulted in smaller particle size and more active defects for HCHO oxidation. Other researchers [30,31] also reported that the presence of carbon matrix during the synthesis process inhibited the growth of MnO_2. However, as we know, it is the first finding that in-situ formed graphite-like nanocarbon matrix intermixes with MnO_2 and inhibits the growth of MnO_2 simultaneously.

3.2. FTIR, Raman spectra and electrochemical property

To learn the effect of carbon decoration on the surface functional groups of as-synthesized carbon-modified MnO_2 samples, FTIR spectra were conducted. The graphite-like and amorphous carbon species are known for their rich surface functional groups [32–34]. As shown in Fig. 3a, a broad absorption at $3390 \, cm^{-1}$ belongs to the O−H stretching vibration, and bands at $~1610 \, cm^{-1}$ and $1384 \, cm^{-1}$ are generally attributed to the −OH group bending vibrations of the water molecules [35]. A medium intensity peak at $1530 \, cm^{-1}$ and a strong peak around $500 \, cm^{-1}$ can be ascribed to the Mn−O lattice vibrations of the [MnO_6] octahedra group [36]. A peak at $1250 \, cm^{-1}$ to −C−O stretching is consistent with carboxyl groups [35]. Comparing the FTIR spectrum of GLC-MnO_2 and AC-MnO_2, it can be found GLC-MnO_2 owned more functional groups of OH, CH and carboxyl.

Fig. 3b shows the Raman spectra of as-synthesized samples. Besides the Raman shift ~310 and $640.5 \, cm^{-1}$ assigned to the vibration of Mn−O bonds [37], the peaks at $1349 \, cm^{-1}$ (D band) and $1591 \, cm^{-1}$ (G band) belong to the graphite-like structure, confirming the presence of graphite-like nanocarbon in the GLC-MnO_2, which may be beneficial for achieving better electric conduction [38]. In comparison with GLC-MnO_2, there are no peaks corresponding to the graphite-like carbon in the AC-MnO_2 sample.

The electrochemical property of as-synthesized samples was also investigated. As shown in Fig. 4a, the GLC-MnO_2 showed a larger cyclic

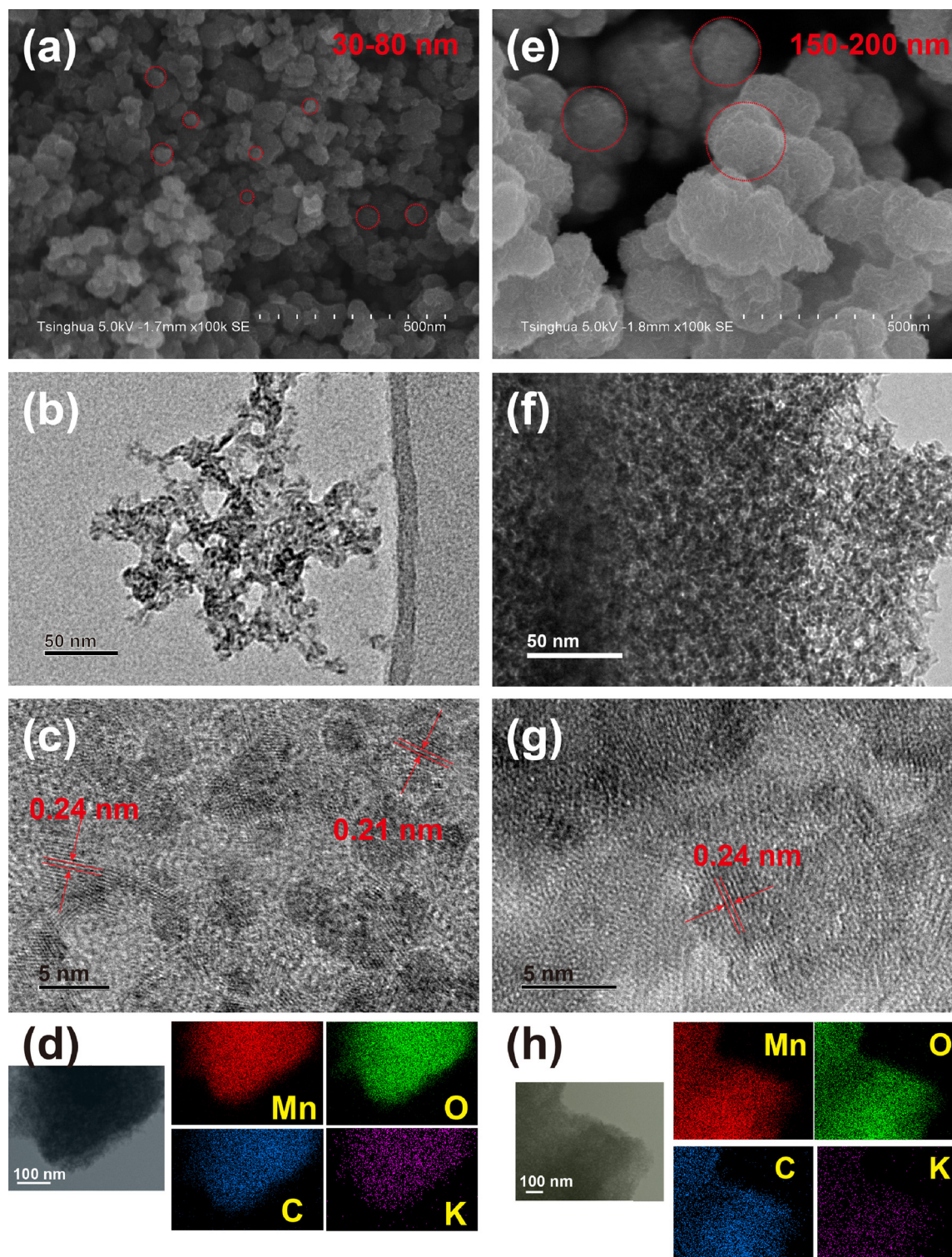**Fig. 2.** SEM, TEM, HR-TEM and EDX mapping results of the GLC-MnO$_2$ (a–d) and AC-MnO$_2$(d–h).

voltammetry (CV) curve area with higher anodic and catholic currents than those of the AC-MnO$_2$ sample. This result indicates that GLC-MnO$_2$ had higher electrical activity than AC-MnO$_2$ sample, which allows an easier path for electrochemical reactions [39,40]. The galvanostatic charge-discharge measurement showed the similar result (Fig. 4b). The GLC-MnO$_2$ needed more charging and discharging time than AC-MnO$_2$, which implied that GLC-MnO$_2$ had more electro-active sites. Initial region of the discharge curve showed a certain potential drop (iR drop), and the iR drop for GLC-MnO$_2$ was smaller than the AC-MnO$_2$,

indicating GLC-MnO$_2$ possessed higher electrochemical conductivity, which facilitates the charge transfer during the redox reaction [41,42].

3.3. XPS and elemental composition

XPS patterns of as-synthesized carbon-modified MnO$_2$ samples are shown in Fig. 5. The Mn 2p$_{3/2}$ spectra are deconvoluted into two peaks with binding energy at 641.8 eV and 642.8 eV corresponding to Mn^{3+} and Mn^{4+}, respectively [43]. After fitting by using XPSPEAK41

Table 1
XPS, ICP-AES and BET results of as-synthesized carbon-modified MnO_2.

Catalysts	Element content (Atomic%)[a]				Atomic ratio				Mn $2p_{3/2}$	Mn 3s	O 1s			C 1s	Surface Area (m^2/g)
	K	Mn	O	C	C/Mn[a]	Mn/O[a]	K/Mn[a]	K/Mn[b]	Mn^{3+}/Mn^{4+}	AOS of Mn[c]	O_α	O_β	O_γ	C_{Oxygen}/C_{total}	
GLC-MnO_2	8.46	21.45	49.00	21.10	0.98	0.44	0.39	0.29	0.72	3.49	0.75	0.20	0.05	0.14	216.0
AC-MnO_2	6.88	22.42	47.18	23.52	1.05	0.48	0.31	0.23	0.64	3.55	0.78	0.15	0.08	0.11	70.3

[a] Calculated from the XPS result.
[b] Calculated from the ICP-AES result.
[c] The average oxidation state (AOS) of Mn was calculated according to an empirical formula (AOS = 8.956 − 1.126 × ΔE).

software, the ratio of Mn^{3+}/Mn^{4+} of GLC-MnO_2 (0.72) was higher than that of AC-MnO_2 (0.64) (Table 1). The higher ratio of Mn^{3+}/Mn^{4+} may facilitate the formation of surface oxygen species [15]. The average oxidation state of Mn derived from the Mn 3s spectra also agrees with the above result. The difference of binding energy (ΔE) between Mn 3s doublet peaks was 4.85 and 4.80 eV (Fig. 5b), the corresponding average oxidation state of Mn was 3.49 and 3.55, respectively [44].

Besides, the O 1s peaks were fitted into three peaks at 529.8, 531.5 and 533 eV (Fig. 5c). The peak at 529.8 eV was assigned to lattice oxygen for Mn−O (denoted as O_α), the peak at 531.5 eV was assigned to surface adsorbed oxygen (denoted as O_β), and the peak at 533 eV was assigned to carbon-related oxygen and oxygen of adsorbed water (denoted as O_γ) [45–47]. The fitting results are shown in Table 1. The GLC-MnO_2 owned the larger content of chemisorbed oxygen than AC-MnO_2 (0.20 vs. 0.15). These surface adsorbed oxygen species such as O_2^-, O^- and OH group have been supposed to play an important role in oxidation reaction process [19,44]. Thus, the abundant surface adsorbed oxygen species owned by GLC-MnO_2 would be beneficial to enhance the activity for HCHO oxidation. The C 1s spectra were deconvoluted into four peaks at 284.6, 285.4, 286.8 and 288.6 eV, corresponding to the bonding of sp^2 C═C, sp^3 C−C, C−O and C═O, respectively (Fig. 5d) [32,48]. The coexistence of sp^2 C and sp^3 C is consistent with the GLC structure as shown in the TEM images, in which the carbon agrees well with the graphite-like structure of sp^2 C, whereas numerous defects indicate the formation of sp^3 C. The occurrence of C═O and C−O mean that various oxygen-containing chemical functional groups are present in the hybrid materials, which is consistent with FTIR results mentioned above.

The surface elemental content determined by XPS is shown in Table 1. GLC-MnO_2 exhibited the smaller Mn/O ratio than AC-MnO_2. The Mn/O ratio of both samples was lower than the stoichiometric ratio of MnO_2 (0.5), indicating the presence of manganese vacancy (V_{Mn}) in the hybrid materials and GLC-MnO_2 owned more abundant V_{Mn} [49,50]. As previously reported by our group [15], the presence of V_{Mn} induced unsaturated oxygen species and K^+ locating nearby V_{Mn} sites facilitated the formation of active oxygen species, accordingly the activity of MnO_2 for HCHO oxidation was greatly improved. In consistent with higher content of V_{Mn} in the GLC-MnO_2 sample, it also owned the

higher amount of K^+ for charge balance as revealed in Table 1. The ratios of K/Mn determined by ICP-AES is somewhat smaller than the corresponding values derived from the XPS analysis. Generally, ICP-AES result reflects the bulk composition, while XPS analysis mainly reflects the surface chemical composition. Thus, the above results imply potassium ions tend to terminate on the surface of the catalysts. It is well known that potassium ions benefit the HCHO oxidation [12,15]. Potassium ions generally locate between layers to compensate the charge imbalance caused by V_{Mn}. Based on the above results, the intermixed graphite-like nanocarbon would increase the content of V_{Mn} and result in more surface adsorbed oxygen species, which are beneficial to enhance the catalytic activity for the HCHO oxidation.

3.4. H_2-TPR, O_2-TPD and ESR

H_2-TPR and O_2-TPD were used to evaluate the reducibility, adsorbed oxygen species in GLC-MnO_2 and AC-MnO_2. As shown in Fig. 6a, the H_2-TPR profiles are deconvoluted into four peaks, defined as α, β, γ and δ, respectively. The α peak is assigned to the consumption of surface adsorbed oxygen species. And β, γ and δ peaks are assigned to successive reductions of $K_xMnO_2 \rightarrow Mn_2O_3 \rightarrow Mn_3O_4 \rightarrow MnO$, respectively [19,51]. The reduction temperature of α peak for GLC-MnO_2 and AC-MnO_2 were 217.9 °C and 227.9 °C, respectively. GLC-MnO_2 exhibited the lower onset reduction temperature, indicating that surface adsorbed oxygen species associated with GLC-MnO_2 were more reducible and reactive.

As shown in Fig. 6b, there are several oxygen desorption peaks in as-synthesized catalysts. The peaks below 400 °C can be assigned to the chemisorbed oxygen molecules and active oxygen species (region I); the peak at 400–600 °C corresponds to O_2 stripped from sub-surface lattice oxygen (region II); and the high temperature desorption peaks (> 600 °C) is related to O_2 desorption from lattice oxygen (region III) [43,47]. Though AC-MnO_2 exhibited a small desorption peak at lower temperature than GLC-MnO_2 in region I, GLC-MnO_2 possessed a much larger and broader desorption peak, which demonstrates that GLC-MnO_2 owned more abundant surface oxygen species with easier mobility. This result is consistent with XPS result mentioned above. The presence of higher amount of adsorbed oxygen species means GLC-
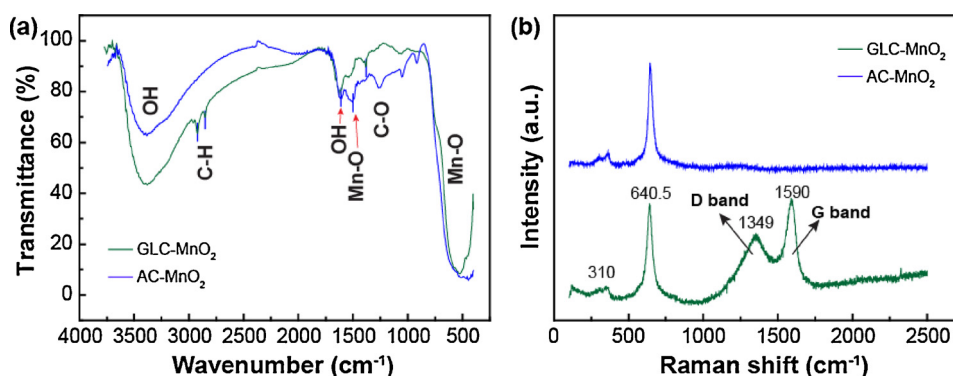

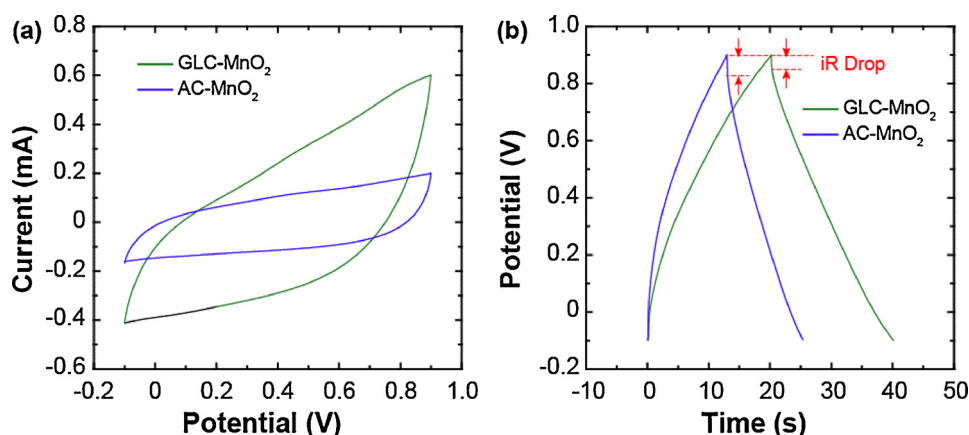**Fig. 3.** (a) FTIR and (b) Raman spectra of GLC-MnO_2 and AC-MnO_2.

Fig. 4. (a) Cyclic voltammograms and (b) galvanostatic charge-discharge curves of GLC-MnO_2 and AC-MnO_2.

MnO_2 can more easily activate O_2 facilitating the oxidation of HCHO.

The ESR spin-trap detection was further used to reveal the reactive oxygen species owned by the catalysts. As shown in Fig. 7, the ESR signals of DMPO-·OH adduct trapped in aqueous solution were observed in both samples, and the signal intensity in the presence of GLC-MnO_2 was much stronger than that in the presence of AC-MnO_2. The signals of DMPO-·O_2^- trapped in the methanol solvent were similar. Both results clearly demonstrate that GLC-MnO_2 owned more active oxygen species like ·OH and ·O_2^- radicals, which may play roles in decomposing HCHO. Recently it is generally recognized that carbonaceous particles may transfer electron to dioxygen to generate reactive oxygen species (ROS) such as superoxide and hydroxyl radicals [52]. Thus, the in-situ formed nanocarbon particles during catalyst preparation not only inhibit the growth of MnO_2 producing more surface defects, but also itself may produce active oxygen species, which are both

beneficial for HCHO oxidation.

3.5. Activity for HCHO removal

Fig. 8 shows the catalytic performance of as-synthesized carbon-decorated MnO_2 for HCHO removal under static test mode. The HCHO concentration decreased very fast in the first 20 min. Within 60 min, the removal ratio by the GLC-MnO_2 catalyst reached 93.5%, which was much higher than that of the AC-MnO_2 catalyst (83.4%). The simultaneous formation of CO_2 during HCHO removal was also detected. Within 60 min, CO_2 concentration in the case of GLC-MnO_2 increased to 140 ppm, which is almost one time higher than that of AC-MnO_2. The CO_2 generation rate by GLC-MnO_2 was much higher than that by layered MnO_2 we previously reported [24], indicating the in-situ formed and intermixed graphite-like nanocarbon greatly enhanced the
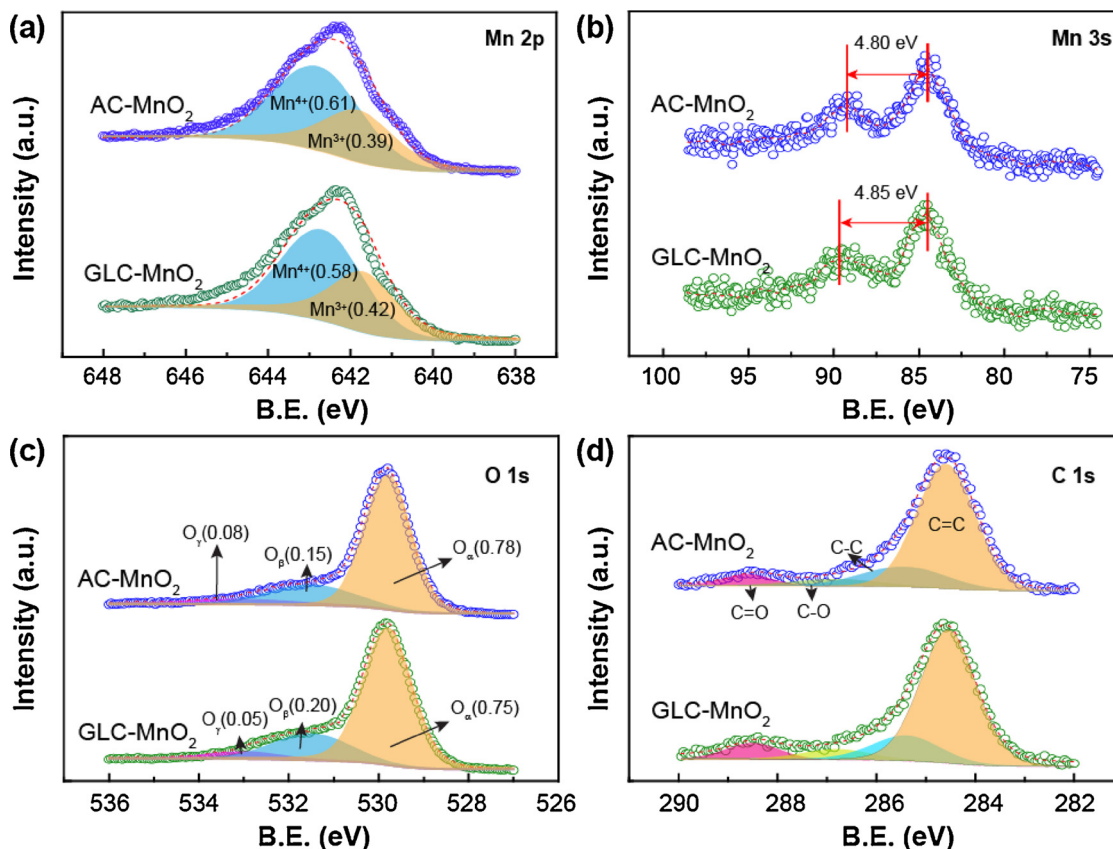

Fig. 5. XPS of GLC-MnO_2 and AC-MnO_2. (a) Mn 2p, (b) Mn 3s, (c) O 1s, (d) C 1s.
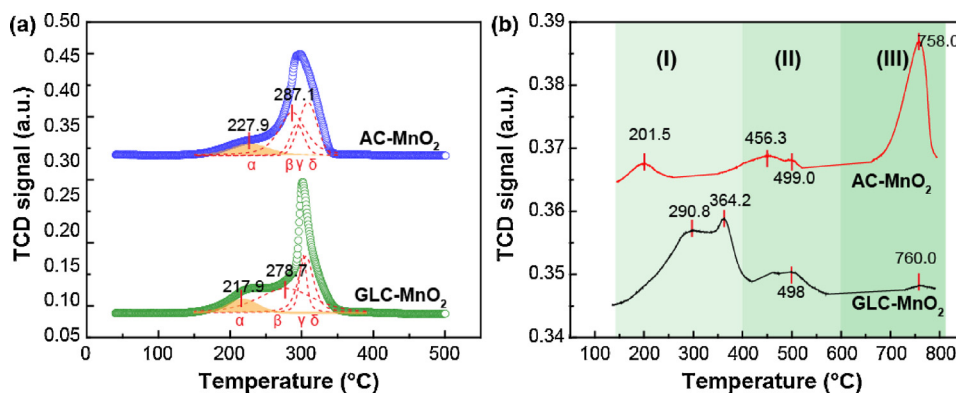
Fig. 6. (a) H_2-TPR and (b) O_2-TPD profiles of the GLC-MnO_2 and AC-MnO_2.
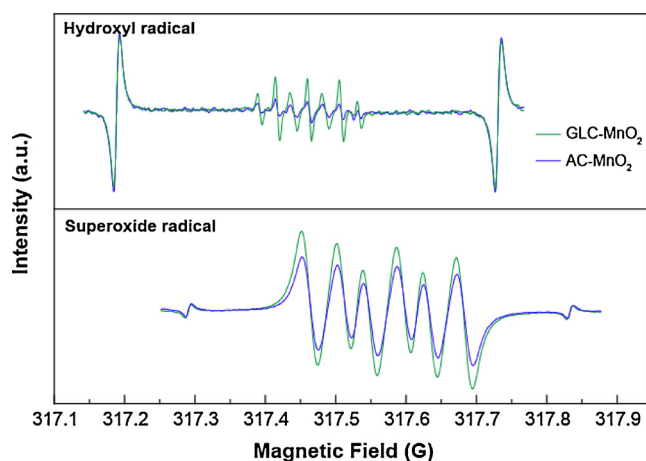

Fig. 7. ESR spectra of radical adducts trapped by DMPO in aqueous (hydroxyl radicals) or methanol (superoxide radicals) suspension in dark at 25 °C.

activity of δ-MnO_2. In addition, we noted the CO_2 generation concentration was somewhat lower than that of removed HCHO, implying that some intermediates formed during HCHO degradation process.

To illustrate the degradation pathway of HCHO on the as-synthesized hybrid MnO_2 materials, in-situ observation of DRIFTS spectra of both samples exposed to a flow of ~80 ppm HCHO/synthetic air within 30 min was conducted at room temperature. As reported in literatures [12,24], generally HCHO is first transformed into dioxymethylene (DOM), then further into formate, carbonate, and finally desorbs as harmless CO_2. As shown in Fig. 9a and b, there is no peak around 1720–1740 cm^{-1}, which is generally assigned to the aldehyde group of HCHO [53,54]. Thus, the HCHO removal contributed by the physical adsorption is little though it contained the intermixed nanocarbon particles. The formation of formate species (1347, 1376–1378,

1571–1592 and 2824–2827 cm^{-1}) and dioxymethylene (DOM) species (1440–1459 cm^{-1}) could be clearly observed on both samples [19,22,55]. The negative broad signals around 3600 cm^{-1} are ascribed to the decrease of surface hydroxyl groups with HCHO exposure time, suggesting that the formation of formate consumed some −OH groups [24]. The peak intensities corresponding to formate and DOM over the GLC-MnO_2 sample were somewhat higher than those over the AC-MnO_2 sample, indicating that HCHO can be degraded faster over the GLC-MnO_2 sample. Besides, the negatively increased intensity of carbonate species (1263 and 1509 cm^{-1}) over the GLC-MnO_2 sample means that carbonate species desorbed more easily from the GLC-MnO_2 catalyst, which is consistent with its higher generation rate of CO_2.

As we know, the World Health Organization (WHO) established an indoor air quality guideline for HCHO of 0.1 mg/m^3 for all 30-min periods at lifelong exposure [56]. And HCHO concentration may be several times higher than the guideline value in polluted indoor environment, but rarely over 1.0 mg/m^3 [57–59]. Thus, it is interesting and more meaningful to evaluate the catalytic activity for low-level HCHO close to the real indoor concentration. Fig. 10 shows the performance of the GLC-MnO_2 sample exposed to the flow of 0.5 mg/m^3 or 1.0 mg/m^3 HCHO under GHSV of 600 L/g_{cat} h at 25 °C, the RH was set at ~55%. The GLC-MnO_2 exhibited excellent activity for low-concentration HCHO under such high space velocity, reaching over 91.8% for 0.5 mg/m^3 and 89.3% for 1.0 mg/m^3 of HCHO. The removal efficiency kept stable during 10 h test.

Moreover, considering the catalyst may be used in dry and very humid indoor environment, we checked the effect of relative humidity on the catalytic activity of GLC-MnO_2 for low-level HCHO removal at room temperature. As shown in Fig. 11, even under extremely dry conditions (RH < 4%), the GLC-MnO_2 catalyst achieved 90.1% removal efficiency for 0.5 mg/m^3 HCHO under GHSV of 600 L/g_{cat} h at 25 °C, which is only a little lower than that under normal humid conditions (RH 55%, 91.8%). When the GLC-MnO_2 catalyst was exposed to very humid conditions (80%), the removal efficiency dropped a little to
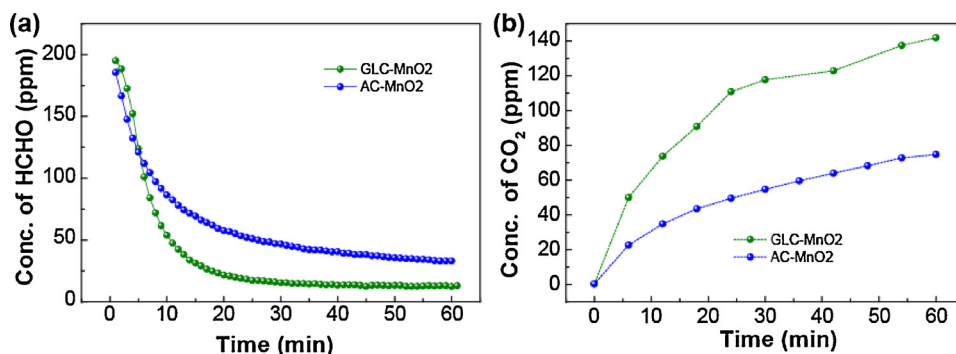

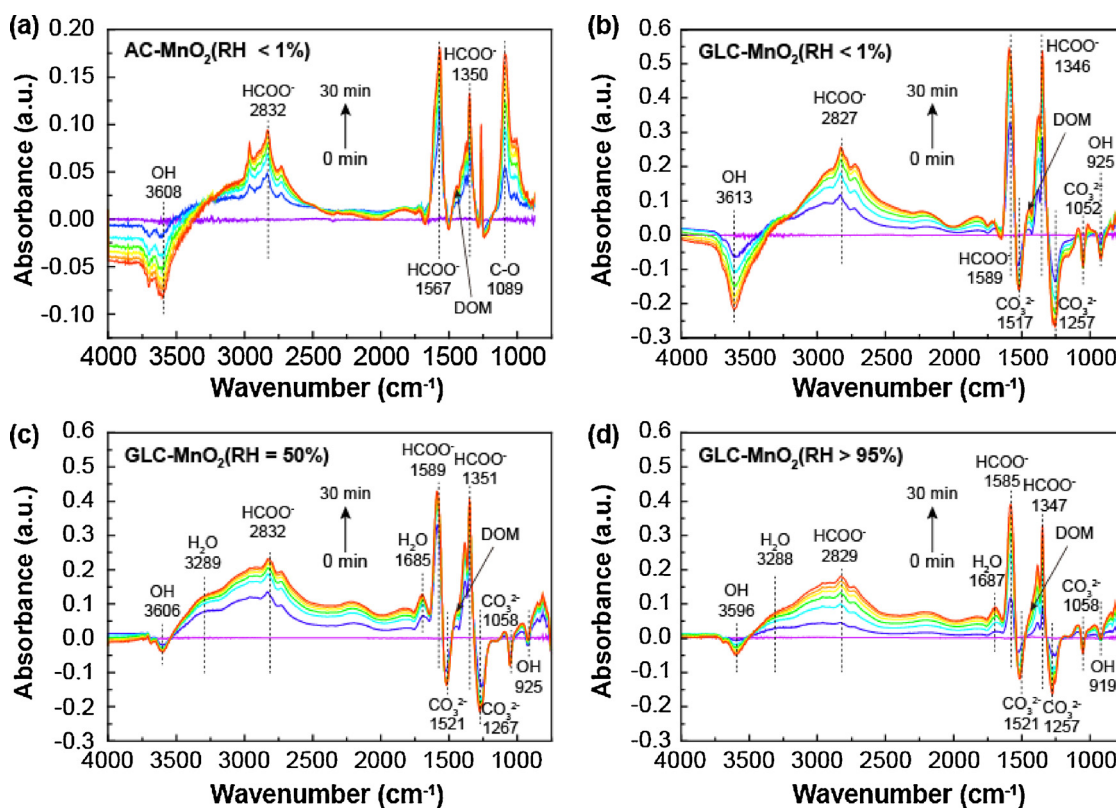**Fig. 8.** The time dependence of (a) HCHO concentration and (b) the generation of CO_2 at 25 °C by GLC-MnO_2 and AC-MnO_2.

Fig. 9. In-situ DRIFTS spectra of AC-MnO$_2$ and GLC-MnO$_2$ samples exposed to the flow of 80 ppm of HCHO/synthetic air with different relative humidity.
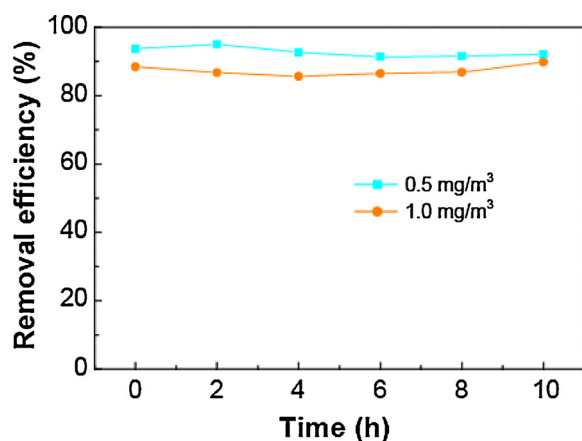

Fig. 10. The removal efficiency of low-concentration HCHO over GLC-MnO$_2$ at 25 °C (GHSV 600 L/g$_{cat}$h, HCHO 0.5 or 1.0 mg/m^3, RH ~55%).
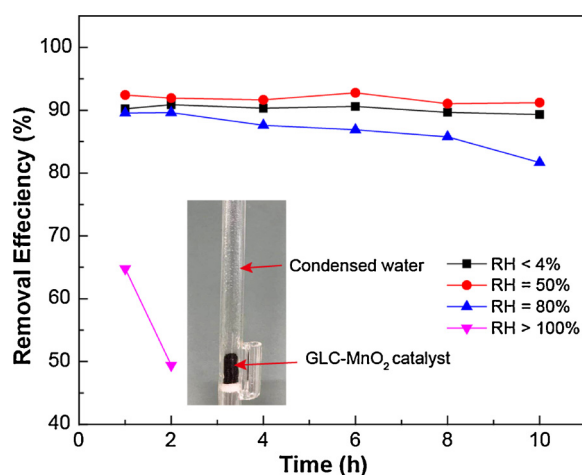

Fig. 11. The removal efficiency of low-concentration HCHO over GLC-MnO$_2$ at 25 °C under different RH (GHSV 600 L/g$_{cat}$ h, HCHO 0.5 mg/m^3). Inset: the photograph of the reaction tube under supersaturated water vapor (RH > 100%) for 2 h.

89% though a slight decrease with time was observed. When the air was supersaturated with water vapor (RH > 100%), the removal efficiency dropped sharply (The 2-h removal efficiency of HCHO is not accurate because HCHO is highly soluble in the water. The reaction was terminated when the water drops was formed.). Based on the above results, it can be concluded that in a wide range of relative humidity (RH 4–80%), as-synthesized GLC-MnO$_2$ catalyst would exhibit a good performance for low-level HCHO at room temperature.

To know the nature of the water vapor effect on the activity, the in-situ DRIFTS of the GLC-MnO$_2$ exposed to a flow of ~80 ppm HCHO/synthetic air under different relative humidity were recorded (Fig. 9b–d). As mentioned above, under dry HCHO condition (RH < 1%), formate species, carbonate species appeared with consumption of surface OH group. When the concentration of water vapor increased (RH 50%), two peaks at 3290 cm^{-1} and 1685 cm^{-1} ascribed to the OH

stretching vibration of water [60,61] increased with time, implying the adsorption of water on the catalyst surface. In the meanwhile, the consumption of surface −OH (3590 cm^{-1}) became weaker than under dry condition, which implies that the water vapor could compensate the surface −OH consumed for HCHO decomposition. When the water vapor concentration further increased to RH > 95%, the intensity of the formate was significantly lowered with accumulation of water on the catalyst surface, indicating the transformation of HCHO into formate was greatly inhibited under RH > 95%. These results indicate that water vapor in air plays at least two roles during HCHO decomposition over the GLC-MnO$_2$ catalyst. Firstly, it adsorbs on the catalyst surface and compensates the surface hydroxyl groups which is

Table 2
Summarization of low-concentration HCHO removal over MnO_2-based catalysts at room temperature.

Catalysts	Test conditions	HCHO removal ratio	Reference
GLC-MnO_2	Fixed-bed reactor; catalyst mass: 0.1 g; HCHO concentration: 0.5 mg/m^3; flow rate: 1.0 L/min; GHSV: 600 L/g$_{cat}$ h, RH: ~55%	92%	this work
	Fixed-bed reactor; catalyst mass: 0.1 g; HCHO concentration: 1 mg/m^3; flow rate: 1.0 L/min; GHSV: 600 L/g$_{cat}$ h, RH: ~55%	89%	
Ce-MnO_2	Fixed-bed reactor; catalyst mass: 0.1 g; HCHO concentration: 0.5 mg/m^3; flow rate: 1.0 L/min; GHSV: 600 L/g$_{cat}$ h, RH: 58 %	~52%	[19]
MnO_x/ honeycomb ceramics	Fixed-bed reactor; HCHO concentration: 1 ppm; flow rate: 52 L/min; GHSV: 48,000 h^{-1}	63%	[21]
MnO_2/AC	Fixed-bed reactor; catalyst mass: 0.5 g; HCHO concentration: 0.5 mg/m^3; flow rate: 1.0 L/min; GHSV: 120 L/g$_{cat}$ h, RH: 45 $\pm$ 5%	90%	[22]
MnO_x/PET	Fixed-bed reactor; catalyst mass: 0.5 g; HCHO concentration: 0.6 mg/m^3; flow rate: 1.0 L/min; GHSV: 120 L/g$_{cat}$	90%	[23]
LBNL-100	0.1 g catalyst loaded on filter media; HCHO concentration: 150–200 ppb; flow rate: 0.1 L/min; GHSV: 60 L/g$_{cat}$ h	~90%	[55]

consumed during HCHO decomposition. This process increases and maintains the activity of the catalyst for the HCHO decomposition. Secondly, water vapor may adsorb competitively with HCHO molecules on catalytic active sites, resulting decrease and even deactivation of catalytic activity.

The performance of reported various MnO_2-based catalysts for low-concentration HCHO at room temperature was summarized in Table 2. Under the high space velocity (GHSV of 600 L/g$_{cat}$ h), Ce-MnO_2 exhibited ~52% removal efficiency at 25 °C [19]. The GLC-MnO_2 hybrid material showed much higher HCHO removal efficiency (~92%) with the same test conditions. The MnO_x/AC catalyst also exhibited high removal efficiency (90%), however the GHSV (120 L/g$_{cat}$ h) adopted for test was much lower than that adopted in this study (600 L/g$_{cat}$ h). Thus, compared with those reported in the literatures, as-synthesized GLC-MnO_2 hybrid material owns the highest catalytic activity for low-concentration HCHO removal at room temperature. It indicates that as-synthesized GLC-MnO_2 have good activity and stability for HCHO removal under such high GHSV condition, which suggest a bright future for practical applications.

Based on the above results, GLC-MnO_2 hybrid materials showed much higher room-temperature activity toward low concentration HCHO than those reported in literatures. Thus, it is a very promising catalytic material for real indoor environment cleaning. Its excellent activity can be ascribed to the following reasons: in-situ formed graphite-like nanocarbon during MnO_2 synthesis inhibits the crystal growth of MnO_2 nanoparticles and separates the primary MnO_2 nanoparticles, accordingly resulting in more defects (e.g., manganese vacancy) and active sites exposed for HCHO oxidation. In addition, the presence of nanometer graphite-like carbon with abundant functional groups may facilitate the formation of reactive oxygen species through electron transfer.

4. Conclusions

In summary, we developed a simple one-step approach to fabricate a graphite-like nanocarbon decorated birnessite-MnO_2 (GLC-MnO_2) composite material. The simultaneous in-situ formed graphite-like nanocarbon limits the growth of MnO_2, resulting in poor crystallinity of MnO_2 and larger specific surface area of the hybrid material. In addition, the amount of manganese vacancies, surface adsorbed active oxygen species and their reducibility were significantly improved. The as-synthesized GLC-MnO_2 displayed superior activity for HCHO removal and its conversation to CO_2. More interestingly, the hybrid GLC-MnO_2 material achieved very high removal efficiency under high GHSV for low-concentration HCHO close to that encountered in the real indoor environment, reaching 92% for 0.5 mg/m^3 of HCHO and 89% for 1.0 mg/m^3 of HCHO at 25 °C under the GHSV of 600 L/g$_{cat}$ h. The water vapor in air could compensate the surface hydroxyl groups on the GLC-MnO_2 catalyst consumed during HCHO decomposition, and it may also competitively adsorb on the reaction active sites to slow down the HCHO decomposition under high relative humidity. However, the GLC-

MnO_2 catalyst showed excellent activity in a wide range relative humidity (4–80%). Thus, the GLC-MnO_2 possesses a great potential for formaldehyde removal in the real indoor environment at room temperature.

References

[1] W. Kanchongkittiphon, M.J. Mendell, J.M. Gaffin, G. Wang, W. Phipatanakul, Indoor environmental exposures and exacerbation of asthma: an update to the 2000 review by the institute of medicine, Environ. Health Perspect. 123 (2015) 6–20.

[2] T. Salthammer, S. Mentese, R. Marutzky, Formaldehyde in the indoor environment, Chem. Rev. 110 (2010) 2536–2572.

[3] M.H. Forouzanfar, L. Alexander, H.R. Anderson, V.F. Bachman, J. Murray, et al., Global, regional, and national comparative risk assessment of 79 behavioural, environmental and occupational, and metabolic risks or clusters of risks in 188 countries, 1990–2013: a systematic analysis for the global burden of disease study 2013, Lancet 386 (2015) 2287–2323.

[4] G.D. Nielsen, P. Wolkoff, Cancer effects of formaldehyde: a proposal for an indoor air guideline value, Arch Toxicol. 84 (2010) 423–446.

[5] J.J. Pei, J.S.S. Zhang, Critical review of catalytic oxidization and chemisorption methods for indoor formaldehyde removal, HVAC&R Res. 17 (2011) 476–503.

[6] J.Q. Torres, S. Royer, J.P. Bellat, J.M. Giraudon, J.F. Lamonier, Formaldehyde: catalytic oxidation as a promising soft way of elimination, ChemSusChem 6 (2013) 578–592.

[7] B.Y. Bai, Q. Qiao, J.H. Li, J.M. Hao, Progress in research on catalysts for catalytic oxidation of formaldehyde, Chin. J. Catal. 37 (2016) 102–122.

[8] X. Hong, Y. Sun, T. Zhu, Z. Liu, Pt-Au/CeO$_2$ catalysts for the simultaneous removal of carbon monoxide and formaldehyde, Catal. Sci. Technol. 6 (2016) 3606–3615.

[9] H. Huang, P. Hu, H. Huang, J. Chen, X. Ye, D.Y.C. Leung, Highly dispersed and active supported Pt nanoparticles for gaseous formaldehyde oxidation: influence of particle size, Chem. Eng. J. 252 (2014) 320–326.

[10] H. Tan, J. Wang, S. Yu, K. Zhou, Support morphology-dependent catalytic activity of Pd/CeO$_2$ for formaldehyde oxidation, Environ. Sci. Technol. 49 (2015) 8675–8682.

[11] J. Zhang, Y. Li, Y. Zhang, M. Chen, L. Wang, C. Zhang, H. He, Effect of support on the activity of Ag-based catalysts for formaldehyde oxidation, Sci. Rep. 5 (2015) 12950–12959.

[12] C. Zhang, F. Liu, Y. Zhai, H. Ariga, N. Yi, Y. Liu, K. Asakura, M. Flytzani-Stephanopoulos, H. He, Alkali-metal-promoted Pt/TiO$_2$ opens a more efficient pathway to formaldehyde oxidation at ambient temperatures, Angew. Chem. Int. Ed. 51 (2012) 9628–9632.

[13] Y. Li, C. Zhang, H. He, J. Zhang, M. Chen, Influence of alkali metals on Pd/TiO$_2$ catalysts for catalytic oxidation of formaldehyde at room temperature, Catal. Sci. Technol. 6 (2016) 2289–2295.

[14] S. Rong, P. Zhang, Y. Yang, L. Zhu, J. Wang, F. Liu, MnO_2 framework for instantaneous mineralization of carcinogenic airborne formaldehyde at room temperature, ACS Catal. 7 (2017) 1057–1067.

[15] J. Wang, J. Li, C. Jiang, P. Zhou, P. Zhang, J. Yu, The effect of manganese vacancy in birnessite-type MnO_2 on room-temperature oxidation of formaldehyde in air, Appl. Catal. B: Environ. 204 (2017) 147–155.

[16] J. Zhang, Y. Li, L. Wang, C. Zhang, H. He, Catalytic oxidation of formaldehyde over manganese oxides with different crystal structures, Catal. Sci. Technol. 5 (2015) 2305–2313.

[17] H. Tian, J. He, X. Zhang, L. Zhou, D. Wang, Facile synthesis of porous manganese oxide K-OMS-2 materials and their catalytic activity for formaldehyde oxidation,

Microporous Mesoporous Mater. 138 (2011) 118–122.

[18] X. Tang, Y. Li, X. Huang, Y. Xu, H. Zhu, J. Wang, W. Shen, MnOx-CeO₂ mixed oxide catalysts for complete oxidation of formaldehyde: effect of preparation method and calcination temperature, Appl. Catal. B: Environ. 62 (2006) 265–273.

[19] L. Zhu, J. Wang, S. Rong, H. Wang, P. Zhang, Cerium modified birnessite-type MnO₂ for gaseous formaldehyde oxidation at low temperature, Appl. Catal. B: Environ. 211 (2017) 212–221.

[20] L. Lu, H. Tian, J. He, Q. Yang, Graphene–MnO₂ hybrid nanostructure as a new catalyst for formaldehyde oxidation, J. Phys. Chem. C 120 (2016) 23660–23668.

[21] M. Wang, L. Zhang, W. Huang, T. Xiu, C. Zhuang, J. Shi, The catalytic oxidation removal of low-concentration HCHO at high space velocity by partially crystallized mesoporous MnOx, Chem. Eng. J. 320 (2017) 667–676.

[22] J. Li, P. Zhang, J. Wang, M. Wang, Birnessite-type manganese oxide on granular activated carbon for formaldehyde removal at room temperature, J. Phys. Chem. C 120 (2016) 24121–24129.

[23] J. Wang, R. Yunus, J. Li, P. Li, P. Zhang, J. Kim, In-situ synthesis of manganese oxides on polyester fiber for formaldehyde decomposition at room temperature, Appl. Surf. Sci. 357 (2015) 787–794.

[24] J. Wang, P. Zhang, J. Li, C. Jiang, R. Yunus, J. Kim, Room-temperature oxidation of formaldehyde by layered manganese oxide: effect of water, Environ. Sci. Technol. 49 (2015) 12372–12379.

[25] X. Peng, Y. Guo, Q. Yin, J. Wu, J. Zhao, C. Wang, S. Tao, W. Chu, C. Wu, Y. Xie, Double-exchange effect in two-dimensional MnO₂ nanomaterials, J. Am. Chem. Soc. 139 (2017) 5242–5248.

[26] H. Ding, S.B. Yu, J.S. Wei, H.M. Xiong, Full-color light-emitting carbon dots with a surface-state-controlled luminescence mechanism, ACS Nano 10 (2016) 484–491.

[27] S. Ghosh, A.M. Chizhik, N. Karedla, M.O. Dekaliuk, I. Gregor, H. Schuhmann, M. Seibt, K. Bodensiek, I.A. Schaap, O. Schulz, A.P. Demchenko, J. Enderlein, A.I. Chizhik, Photoluminescence of carbon nanodots: dipole emission centers and electron-phonon coupling, Nano Lett. 14 (2014) 5656–5661.

[28] J. Zhou, L. Qin, W. Xiao, C. Zeng, N. Li, T. Lv, H. Zhu, Oriented growth of layered-MnO₂ nanosheets over α-MnO₂ nanotubes for enhanced room-temperature HCHO oxidation, Appl. Catal. B: Environ. 207 (2017) 233–243.

[29] Y. Meng, W. Song, H. Huang, Z. Ren, S.Y. Chen, S.L. Suib, Structure-property relationship of bifunctional MnO₂ nanostructures: highly efficient, ultra-stable electrochemical water oxidation and oxygen reduction reaction catalysts identified in alkaline media, J. Am. Chem. Soc. 136 (2014) 11452–11464.

[30] Y. Qin, J. Lu, P. Du, Z. Chen, Y. Ren, T. Wu, J.T. Miller, J. Wen, D.J. Miller, Z. Zhang, K. Amine, In situ fabrication of porous-carbon-supported α-MnO₂ nanorods at room temperature: application for rechargeable Li-O₂ batteries, Energy Environ. Sci. 6 (2013) 519.

[31] R. Zou, Z. Zhang, L. Yu, Q. Tian, Z. Chen, J. Hu, A general approach for the growth of metal oxide nanorod arrays on graphene sheets and their applications, Chem. Eur. J. 17 (2011) 13912–13917.

[32] X. Zhou, X. Wang, X. Feng, K. Zhang, X. Peng, H. Wang, C. Liu, Y. Han, H. Wang, Q. Li, Loading Cd0.5Zn0.5S quantum dots onto onion-like carbon nanoparticles to boost photocatalytic hydrogen generation, ACS Appl. Mater. Interfaces 9 (2017) 22560–22567.

[33] P. Shi, L. Li, L. Hua, Q. Qian, P. Wang, J. Zhou, G. Sun, W. Huang, Design of amorphous manganese oxide@multiwalled carbon nanotube fiber for robust solid-state supercapacitor, ACS Nano 11 (2017) 444–452.

[34] R.J. Cullen, D.R. Jayasundara, L. Soldi, J.J. Cheng, G. Dufaure, P.E. Colavita, Spontaneous grafting of nitrophenyl groups on amorphous carbon thin films: a structure-reactivity investigation, Chem. Mater. 24 (2012) 1031–1040.

[35] Y. Wu, P. Wei, S. Pengpumkiat, E.A. Schumacher, V.T. Remcho, Development of a carbon dot (C-Dot)-linked immunosorbent assay for the detection of human alpha-fetoprotein, Anal. Chem. 87 (2015) 8510–8516.

[36] S. Mallakpour, M. Madani, Use of valine amino acid functionalized α-MnO₂/chitosan bionanocomposites as potential sorbents for the removal of lead(II) ions from aqueous solution, Ind. Eng. Chem. Res. 55 (2016) 8349–8356.

[37] C.H. Chen, E.C. Njagi, S.Y. Chen, D.T. Horvath, L. Xu, A. Morey, C. Mackin, R. Joesten, S.L. Suib, Structural distortion of molybdenum-doped manganese oxide octahedral molecular sieves for enhanced catalytic performance, Inorg. Chem. 54 (2015) 10163–10171.

[38] C. He, S. Wu, N. Zhao, C. Shi, E. Liu, J. Li, Carbon-encapsulated Fe₃O₄ nanoparticles as a high-rate lithium ion battery anode material, ACS Nano 7 (2013) 4459–4469.

[39] A.N. Banerjee, V.C. Anitha, S.W. Joo, Improved electrochemical properties of morphology-controlled titania/titanate nanostructures prepared by in-situ hydrothermal surface modification of self-source Ti substrate for high-performance

[40] J.T. Mefford, W.G. Hardin, S. Dai, K.P. Johnston, K.J. Stevenson, Anion charge storage through oxygen intercalation in LaMnO₃ perovskite pseudocapacitor electrodes, Nat. Mater. 13 (2014) 726–732.

[41] S. Gomez-Carretero, B. Libberton, M. Rhen, A. Richter-Dahlfors, Redox-active conducting polymers modulate Salmonella biofilm formation by controlling availability of electron acceptors, NPJ Biofilms Microbiomes 3 (2017) 19–28.

[42] L. Hao, J. Ning, B. Luo, B. Wang, Y. Zhang, Z. Tang, J. Yang, A. Thomas, L. Zhi, Structural evolution of 2D microporous covalent triazine-based framework toward the study of high-performance supercapacitors, J. Am. Chem. Soc. 137 (2015) 219–225.

[43] J. Jia, P. Zhang, L. Chen, Catalytic decomposition of gaseous ozone over manganese dioxides with different crystal structures, Appl. Catal. B: Environ. 189 (2016) 210–218.

[44] J. Jia, P. Zhang, L. Chen, The effect of morphology of α-MnO₂ on catalytic decomposition of gaseous ozone, Catal. Sci. Technol. 6 (2016) 5841–5847.

[45] S. Rong, P. Zhang, J. Wang, F. Liu, Y. Yang, G. Yang, S. Liu, Ultrathin manganese dioxide nanosheets for formaldehyde removal and regeneration performance, Chem. Eng. J. 306 (2016) 1172–1179.

[46] Y. Wang, C. Ge, L. Zhan, C. Li, W. Qiao, L. Ling, MnOx-CeO₂/activated carbon honeycomb catalyst for selective catalytic reduction of NO with NH₃ at low temperatures, Ind. Eng. Chem. Res. 51 (2012) 11667–11673.

[47] H. Wang, H. Arandiyan, H.A. Tahini, J. Scott, X. Tan, H. Dai, J.D. Gale, A.L. Rohl, S.C. Smith, R. Amal, The controlled disassembly of mesostructured perovskites as an avenue to fabricating high performance nanohybrid catalysts, Nat. Commun. 8 (2017) 15553–15560.

[48] Y.X. Pan, Y. You, S. Xin, Y. Li, G. Fu, Z. Cui, Y.L. Men, F.F. Cao, S.H. Yu, J.B. Goodenough, Photocatalytic CO₂ reduction by carbon-coated indium-oxide nanobelts, J. Am. Chem. Soc. 139 (2017) 4123–4129.

[49] H. Wang, J. Zhang, X. Hang, X. Zhang, Xie J, B. Pan, Y. Xie, Half-metallicity in single-layered manganese dioxide nanosheets by defect engineering, Angew. Chem. Int. Ed. 54 (2015) 1195–1199.

[50] S. Rong, K. Li, P. Zhang, F. Liu, J. Zhang, Potassium associated manganese vacancy in birnessite-type manganese dioxide for airborne formaldehyde oxidation, Catal. Sci. Technol. 8 (2018) 1799–1812.

[51] J. Wang, D. Li, P. Li, P. Zhang, Q. Xu, J. Yu, Layered manganese oxides for formaldehyde-oxidation at room temperature: the effect of interlayer cations, RSC Adv. 5 (2015) 100434–100442.

[52] J.J. Pignatello, W.A. Mitch, W.Q. Xu, Activity and reactivity of pyrogenic carbonaceous matter toward organic compounds, Environ. Sci. Technol. 51 (2017) 8893–8908.

[53] X. Cao, M.A. Tarr, Aldehyde and ketone photoproducts from solar-irradiated crude oil-seawater systems determined by electrospray ionization-tandem mass spectrometry, Environ. Sci. Technol. 51 (2017) 11858–11866.

[54] R. Ding, C. Wolf, Catalytic insertion of aldehydes into dihalonitroacetophenones via sequential bond scission-aldol reaction-acyl transfer, Chem. Commun. 52 (2016) 3576–3579.

[55] X. Wang, Z. Lan, K. Zhang, J. Chen, L. Jiang, R. Wang, Structure-activity relationships of AMn₂O₄ (A = Cu and Co) spinels in selective catalytic reduction of NOx: experimental and theoretical study, J. Phys. Chem. C 121 (2017) 3339–3349.

[56] G.D. Nielsen, S.T. Larsen, P. Wolkoff, Re-evaluation of the WHO (2010) formaldehyde indoor air quality guideline for cancer risk assessment, Arch. Toxicol. 91 (2017) 35–61.

[57] X.J. Tang, Y. Bai, A. Duong, M.T. Smith, L. Li, L.P. Zhang, Formaldehyde in China: production, consumption, exposure levels, and health effects, Environ. Int. 35 (2009) 1210–1224.

[58] C. Jiang, S. Li, P. Zhang, J. Wang, Pollution level and seasonal variations of carbonyl compounds, aromatic hydrocarbons and TVOC in a furniture mall in Beijing, China, Build. Environ. 69 (2013) 227–232.

[59] M. Weng, L. Zhu, K. Yang, S. Chen, Levels and health risks of carbonyl compounds in selected public places in Hangzhou, China, J. Hazard. Mater. 164 (2009) 700–706.

[60] M.A. Sidheswaran, H. Destaillats, D.P. Sullivan, J. Larsen, W.J. Fisk, Quantitative room-temperature mineralization of airborne formaldehyde using manganese oxide catalysts, Appl. Catal. B: Environ. 107 (2011) 34–41.

[61] D.W. Kwon, P.W. Seo, G.J. Kim, S.C. Hong, Characteristics of the HCHO oxidation reaction over Pt/TiO₂ catalysts at room temperature: the effect of relative humidity on catalytic activity, Appl. Catal. B: Environ. 163 (2015) 436–443.

supercapacitors, Sci. Rep. 7 (2017) 13227–13246.